



Landsat-derived impervious surface area expansion in the Arctic from 1985 to 2021

Zhengrong Liu^a, Jie Yang^{a,*}, Xin Huang^{a,b}

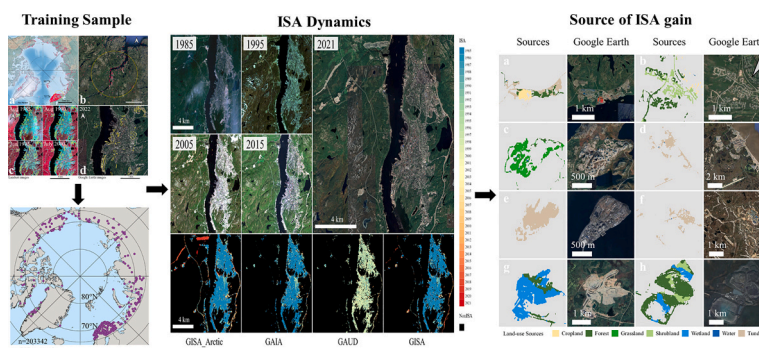
^a School of Remote Sensing and Information Engineering, Wuhan University, Wuhan 430079, PR China

^b State Key Laboratory of Information Engineering in Surveying, Mapping and Remote Sensing, Wuhan University, Wuhan 430079, PR China

HIGHLIGHTS

- The 30-m impervious surface areas (ISA) dataset for the Arctic Circle
- We proposed a sample generation strategy for sparse ISA coverage.
- Omission error, commission error and F-score is 8.70 %, 4.31 % and 0.93, respectively
- Arctic ISA reached 2115.49 km² by 2021, more than 1.46 times that of 1985.
- The tundra represents the primary source (over one-third) of ISA expansion.

GRAPHICAL ABSTRACT



ARTICLE INFO

Editor: Shuqing Zhao

Keywords:
 Impervious surface
 Landsat
 Arctic
 Google Earth Engine
 Urban

ABSTRACT

Accurate and timely impervious surface mapping is essential for assessing land cover change, urban heat island, and monitoring human activity intensity and ecological change. While various global impervious surface datasets become available, these datasets exhibit significant omissions in Arctic regions. Hence, in this study, we present a 30-m impervious surface area (ISA) dataset of Arctic from 1985 to 2021 (GISA_Arctic). To this aim, we proposed to combine visually interpreted ISA samples and automatically generated NonISA samples for Arctic ISA mapping. Then, adaptive random forest (RF) classifiers were used for long time-series ISA mapping and the result was post-processed to improve the spatial-temporal consistency. Finally, the accuracy of GISA_Arctic was assessed using the 37,800 independent test samples. GISA_Arctic possessed an overall accuracy of 93.59 % and a F-score of 0.934. It is found that the Arctic ISA increased from 857.83 km² to 2115.49 km² during the past 37 years. More than 84 % of the Arctic ISA increment is embraced by three countries: Russia, Finland, and Norway. Courtesy of the long time-series GISA_Arctic, the sources of Arctic ISA expansion were further analyzed. It was found that the top three land covers transformed to ISA are tundra, forest and grassland. The GISA_Arctic could contribute to further understanding of human activities and Arctic ecological changes, which can be accessed from http://irsi.p.wuhan.edu.cn/resources/resources_v2.php.

* Corresponding author.

E-mail address: yang9tn@163.com (J. Yang).

<https://doi.org/10.1016/j.scitotenv.2023.166966>

Received 18 June 2023; Received in revised form 14 August 2023; Accepted 8 September 2023

Available online 17 September 2023

0048-9697/© 2023 Elsevier B.V. All rights reserved.

1. Introduction

Since the 1970s, rapid economic and population growth has led to increased human activities and ISA dynamics, exacerbating the deterioration of the hydrological cycle, biodiversity, agricultural production and livelihood, and other ecosystem issues (Weng, 2012) (Seto et al., 2012). ISA refers to artificial structures that prevent water permeation into the soil, including asphalts, concrete, sand and stone, mines etc. (Chen et al., 2015). Over the past half-century, global ISA has expanded rapidly by approximately 0.62 million km² from 1972 to 2019 (Huang et al., 2021b). Meanwhile, human activities such as energy exploitation, construction of shipping and air transport facilities, and expansion of residential areas have significantly increased ISA in the Arctic (Usman et al., 2022) (Nguyen et al., 2021) (Lifshits et al., 2021). The Arctic is undergoing significant ecosystem changes, such as permafrost degradation, sea ice melting, and northward forest expansion, due to the climate change and human activities (Chen et al., 2022) (Guo et al., 2018) (Hermosilla et al., 2019) (Overland et al., 2014). Given the importance of Arctic ecosystems for global energy exchange and carbon cycling, the impacts of rapid changes in Arctic ecology extend from the regional ecosystem to the global scale (McGuire et al., 2009) (Schoor et al., 2015) (Assessment, 2005). Therefore, timely monitoring of Arctic ISA dynamic is crucial for understanding water-carbon cycle, biodiversity, global climate and environmental changes.

Remote sensing is an essential tool for ecosystem monitoring that has the capability of scanning Earth surface over long time-series and wide coverage (Beamish et al., 2020). There have been many studies focusing on ISA mapping using coarse-resolution imagery. For instance, Liu et al. (2012) obtained 1000-m urban information for China from 1992 to 2008 by calibrated Defense Meteorological Satellite Program's Operational Line-scan System (DMSP-OLS) nighttime lighting data (NTL). Similarly, Zhou et al. (2018) proposed an adaptive thresholding method using DMSP-OLS NTL data to obtain global long time-series urban extent. Moreover, Schneider et al. (2010) used 500-m Moderate Resolution Imaging Spectroradiometer (MODIS) data to map annual global urban dynamic based on ecological zone layers. Huang et al. (2021a) also mapped global urban area using MODIS data based on an automated sampling strategy. However, coarse-resolution imagery makes it difficult to delineate detailed urban environment. Therefore, ISA mapping with the fine spatial resolution data (e.g., 30-m Landsat) has drawn more attention in the literature. For example, Sexton et al. (2013) used Landsat archives to delineate annual ISA dynamics over metropolitan regions, while Zhang et al. (2017) used a fuzzy clustering method to depict ISA dynamic from monthly Landsat composites.

The limitations of storage and computation capacity have led many studies to rely on single-source remote sensing datasets or to focus on limited spatial extent. However recent advancements in cloud computing platform, such as Google Earth Engine (GEE), have enabled time-series ISA mapping over large scales by providing access to petabytes of remote sensing data and high-performance parallel computing services (Gorelick et al., 2017). For instance, Liu et al. (2020) used Landsat images on the GEE platform to unveil Global Annual Urban Dynamics (GAUD) (1985–2015) utilizing the Normalized Urban Areas Composite Index (NUACI) and a temporal segmentation method. Similarly, Gong et al. (2020) developed Global Artificial Impervious Area (GAIA) using Landsat archives on the GEE to document annual global ISA dynamics. Meanwhile, Huang et al. (2021b) generated the first 30-m Global Impervious Surface Area (GISA) from 1972 to 2019 using a distributed processing framework, with its successor (i.e., GISA 2.0) improving upon the inconsistent regions using a semi-automated sample strategy (Huang et al., 2022a). Therefore, it is practical to use the GEE platform for large-scale and time-series Arctic ISA mapping.

In addition to long time-series ISA datasets, recent studies also focus on global ISA mapping at 10 m. For instance, Marconcini et al. (2020) produced a global 10-m residential layer (World Settlement Footprint, WSF) based on support vector machine using Landsat and Sentinel data.

Besides, Corbane et al. (2021) generated a new Global Human Settlement Layer (GHSL2018) using a convolutional neural network based on Sentinel-2 multispectral data. Meanwhile, Huang et al. (2022b) et al. developed a 10 m global ISA dataset (GISA-10m) using automated samples based on multi-source geospatial data. Although there have been many large-scale and time-series ISA mapping studies, ISA mapping over Arctic region remains challenging due to issues such as short summer sunlight duration and small viewing zenith angle. In addition, Arctic ISA is scattered, making it difficult to collect training samples. Moreover, the existing global time-series ISA datasets show relatively more omissions over the Arctic region. Therefore, new and accurate time-series ISA mapping is required to address the aforementioned issues.

In order to address the aforementioned deficiencies, we developed a new 30-m ISA dataset for Arctic Circle (i.e., areas with latitude greater than 66°34'N) for 1985–2021 using 337,799 Landsat images, namely GISA_Arctic. To this end, the ISA and non-impervious surface (NonISA) training samples were first collected based on satellite images (e.g., Landsat, Google Earth) and crowdsourcing data (OpenStreetMap, Geonames) through visual interpretation. The Arctic Circle was further subdivided into 412 hexagons, where adaptive RF classification and post-processing were performed to ensure spatiotemporal consistency of the results. The performance of GISA_Arctic was assessed using 37,800 independent samples and compared with three existing datasets (i.e., GAIA, GAUD, GISA). Finally, the sources of Arctic ISA expansion were further analyzed. In conclusion, this manuscript endeavors to introduce a novel approach for generating ISA training sample sets, establish a comprehensive long time-series ISA dataset for the Arctic, and shed light on the drivers of ISA expansion in this unique and ecologically fragile region. Through addressing data gaps and offering essential temporal insights, this research provides a valuable understanding of long-term ISA dynamics. This, in turn, facilitates the exploration of human activity intensity within the Arctic domain and its far-reaching implications for ecosystem evolution.

2. Data

2.1. Landsat

All available 30-m Landsat 5, 7, and 8 images covering the Arctic region from 1985 to 2021 were used in GISA_Arctic mapping. Landsat 5 was processed using the Landsat Ecosystem Disturbance Adaptive Processing System (LEDAPS) algorithm (Schmidt et al., 2013), while Landsat 8 was corrected by the Land Surface Reflectance Code (LaSRC) method (Vermote et al., 2016). Clouds, shadows, water and snow in the Landsat data were removed by CFMASK algorithm (Zhu et al., 2015).

2.2. Auxiliary data

2.2.1. Digital elevation data

Topographic variables such as elevation, slope and aspect are frequently employed to describe terrain changes in ISA mapping (Huang et al., 2021b). In this study, we used topographic features derived from the 250-m Global Multi-Resolution Terrain Elevation Data 2010 (GMTED2010) to describe the ISA distribution across various topographic characteristics. The GMTED2010 data is based on Shuttle Radar Topographic Mission Terrain (SRTM), incorporating a variety of other data sources to improve coverage.

2.2.2. Night light data

NTL data, which captures surface light intensity, is commonly used as a proxy for human activity and economic development in ISA mapping (Zhou et al., 2018) (Gong et al., 2020). In this study, we used the annual median from NTL data provided by the Visible Infrared Imaging Radiometer Suite (VIIRS) with a spatial resolution of 15 arc sec (~ 500 m) in 2020 to address the issue of overestimation resulting from spectral

confusion between bare soils and ISA (Elvidge et al., 2017) (Mills et al., 2013).

2.2.3. MODIS data

To improve the saturation of NTL, we utilized the MYD13Q1 in 2020 on GEE. The MYD13Q1 V6 product provides a 16-day compositing Enhanced Vegetation Index (EVI) with a spatial resolution of 250 m. This product has undergone atmospheric correction to minimize the impacts of water, clouds, heavy aerosols, and shadows (Clinton and Gong, 2013).

2.2.4. OpenStreetMap

The OpenStreetMap (OSM) project was developed to provide the general public with free, editable, and open-source internet maps that can be used for driving directions, three-dimensional (3D) city models, and landcover classification (Fonte et al., 2020; Goetz, 2013; Haklay and Weber, 2008; Tian et al., 2019). Millions of contributors worldwide have compiled this emerging crowd-sourced map (Haklay and Weber, 2008). Furthermore, numerous building and road labels in ISA mapping have been derived from OSM after cleaning (Lin et al., 2020). In this study, OSM in 2021 was used to filter out errors in the potentially NonISA samples.

2.2.5. GeoNames

GeoNames stands as an accessible and open-source global database of place names, encompassing 2.8 million residences and 5 million alternative names. This comprehensive dataset provides an array of attributes for each place name, including longitude and latitude coordinates, administrative divisions, population statistics, and other pertinent features. The geographical coverage of GeoNames is extensive, encompassing numerous urban and rural settlements. In this study, 21,827 points sourced from GeoNames in 2021 within the Arctic Circle were employed to identify potential ISA training samples.

2.2.6. GlobeLand30

This study leveraged the 30-m GlobeLand30 land cover data in 2000 and 2020. The GlobeLand30 was developed through the integration of pixel, object, and expert knowledge methods, incorporating substantial manual interpretation to refine the mapping results (Chen et al., 2015). The dataset encompasses ten distinct land cover categories, specifically arable land, forest land, grassland, shrubs, wetlands, water bodies, tundra, ISA, bare land, glaciers, and permanent snow cover. Notably, the GlobeLand30 dataset has been reported to exhibit an overall accuracy of 80.3 %.

2.3. Existing ISA data

In this study, the performance of GISA_Arctic was compared with existing 30-m ISA products (i.e., GAIA, GAUD, and GISA) and 10-m ISA products (i.e., WSF2015, GHSL2018, GISA-10m). GAIA is a global 30-m annual ISA product covering the period from 1985 to 2018. It was produced using the “Exclusion-Inclusion” algorithm (Gong et al., 2020) (Li and Gong, 2016), which employed Sentinel-1 and NTL data to mitigate the overestimation of ISA in arid regions. The average overall accuracy of GAIA was reported over 89 %.

GAUD used automatically collected training samples from high-confidence urban areas and RF classification method to obtain global urban extent in 1985 and 2015. Then, the year of urban expansion or shrink was identified using a regression-based temporal segmentation method. Based on 12,000 visually-interpreted test samples, the overall accuracy for GAUD was 76 % (1985–2000) and 82 % (2000–2015), respectively (Liu et al., 2020).

GISA is a 30-m global ISA dataset from 1972 to 2019 that performed temporal post-processing to improve spatial-temporal consistence. The GISA was validated based on 120,777 samples, with omission error, commission error and F-score of 5.16 %, 0.82 % and 0.954, respectively

(Huang et al., 2021b).

WSF2015 used automated training samples and temporal and texture features to obtain global human settlements map. And a series of post-processing steps were conducted based on multi-source data to automatically identify and delete false alarms. According to the evaluation of the test set obtained from crowdsourcing data, the average accuracy of WSF2015 is 89.33 % (Marconcini et al., 2020).

GHSL2018 is a global 10-m residential layer generated through deep learning methods using Sentinel-2 annual multispectral data. Employing multi-source training samples and transfer learning strategies, GHSL2018 comprehensively delineates the distribution of ISA within residential settings. According to independent validation samples from 277 regions of interest, the overall accuracy (using 0.2 as the threshold) is greater than 75 % (Corbane et al., 2021).

GISA-10m constitutes a global 10-m ISA dataset in 2016 (Huang et al., 2022b). This product employs an automated sample generation strategy, creating 58 million samples through existing ISA datasets and crowdsourcing data. The GISA was validated based on 10,800 samples, with overall accuracy, F-score and kappa of 86.19 %, 77.96 % and 0.679, respectively (Huang et al., 2022b).

All the above data were processed on GEE. The distinctive digital pyramid structure of GEE enables the fusion of data originating from varying temporal and spatial resolutions, contributing to the efficient data processing (Gorelick et al., 2017).

3. Methodology

Fig. 1 illustrates the mapping framework of GISA_Arctic, including sample generation, multi-source features extraction, adaptive RF classification, spatiotemporal post-processing, and accuracy assessment.

3.1. Training sample generation

Although Huang et al. (2021b) has demonstrated the feasibility to acquire training samples from existing datasets via specific rules, it is difficult to collect ISA samples automatically in Arctic due to the large omission of existing datasets. Therefore, in this study visual interpretation with a series of spatial rules is utilized to generate training samples.

In general, the diversity of training samples affects the generalization performance of the classifier. Therefore it requires enormous and widely distributed samples to ensure the mapping result (Gómez et al., 2016). However, it is time-consuming and laborious to visually search for potential ISA training samples over vast Arctic. To deal with this challenge, we attempted to locate possible ISA from GeoNames and OSM (mining areas, airports, etc.). GeoNames is a widely used toponymic dataset that collects global human settlements, names and coordinates information. In such a way, we can quickly locate potential ISA training samples. Taking Fig. 2b as an example, with reference to GeoNames, we successfully located the ISA in Murmansk, Russia. Then, potential ISA areas (yellow box in Fig. 2c&d) were outlined by interpretation from the earliest Landsat data available on GEE (Fig. 2c). In addition, we also checked the time-series vegetation index curves (obtained from Landsat and MODIS) to ensure the temporal stability of ISA training samples. Subsequently, spatial rules were applied to further filter the samples: (1) A 15 m buffer (about half of a Landsat pixel) was generated inward from the potential ISA sample area to reduce the influence of edge pixels; (2) We randomly sampled the obtained potential ISA with the distance between them greater than 100 m to ensure the spatial independence; (3) Additional verification via high-resolution Google Earth images (mainly after 2000) was performed to improve the reliability of samples.

Compared to the sparse ISA samples, the NonISA samples are more widely distributed. Therefore, we employed an automated strategy to generate NonISA samples. Firstly, we created a potential pool of NonISA sample from regions labeled as NonISA by existing datasets (i.e., GAIA, GAUD, and GISA). In order to increase the accuracy of the NonISA

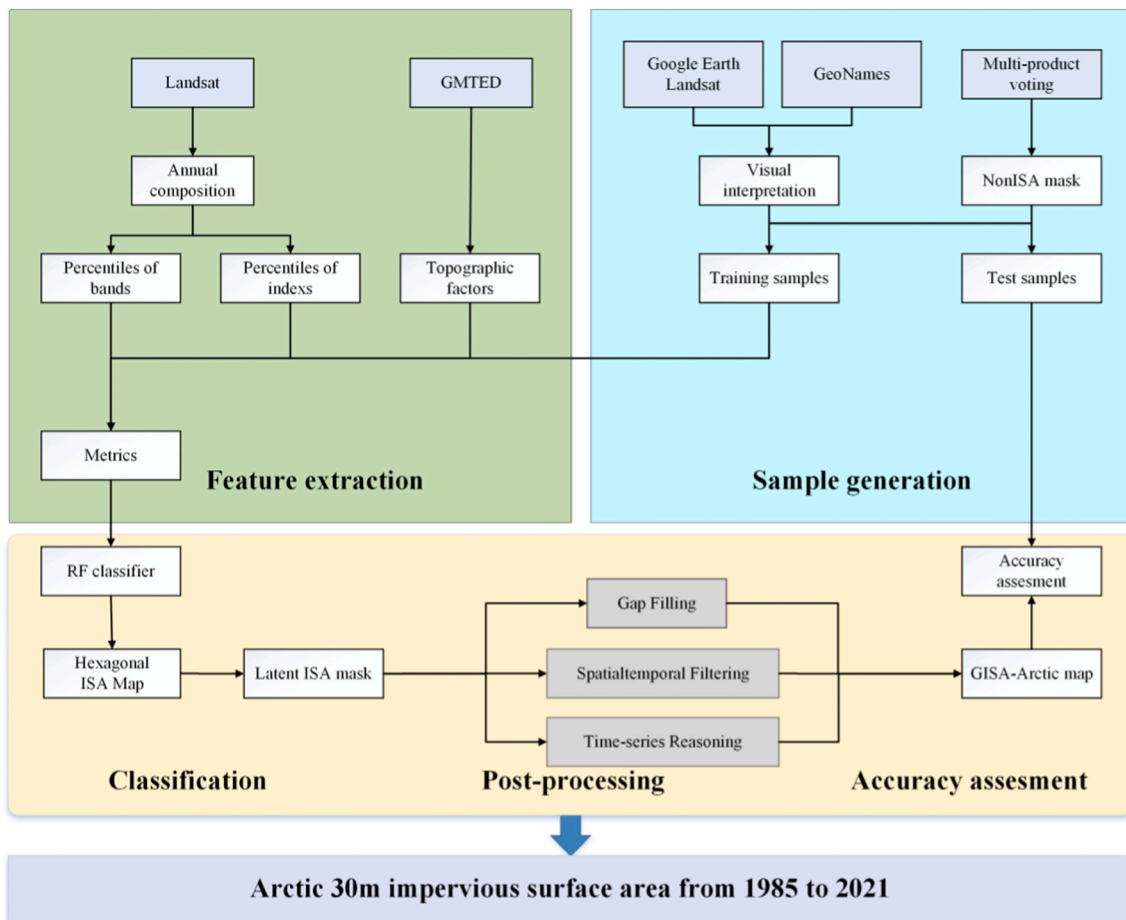


Fig. 1. The framework of GISA_Arctic mapping in this study.

samples, some latest ISA datasets were also taken into consideration, such as OSM, WSF2015 (Marconcini et al., 2020), GHSL2018 (Corbane et al., 2021), GlobeLand30 2020 (Chen et al., 2015) and GISA-10m (Huang et al., 2022b). This approach of combining these ISA datasets with the buildings and roads (mainly from the OSM) could effectively reduce the ISA omissions. Finally, NonISA samples were randomly generated within the potential sample pool and their quality was further ensured through visual inspection. In this way, we obtained 1,220,052 training samples in the Arctic, including 203,342 ISA samples and 1,016,710 NonISA samples.

3.2. Feature extraction and classification

In the case of large-scale ISA mapping, the study region is usually divided into multiple sub-regions to better delineate the heterogeneous landscape. Therefore, we divided the Arctic with hexagons to ensure the mapping performance (Huang et al., 2022b). For each mapping grid (i.e., hexagon), a locally adaptive RF classifier was built with input features including spectrum, spectral difference index, phenology, and topography. Specifically, a total of 48 features were extracted from multi-source data, i.e., 18 spectral responses, 24 normalized indices, 3 temporal statistics, and 3 topographic features (Table 1). Above all, the 20th, 50th, and 80th percentile of spectral features were obtained from all available Landsat images. In such a way, we could retain the time-series information while reduce the contamination from clouds and shadows. Based on the above annual spectral percentages, we calculated 8 normalized indices for ISA mapping, namely the Normalized Difference Vegetation Index (NDVI) (Rouse Jr et al., 1973), Normalized Difference Snow Index (NDSI) (Hall et al., 1995), Normalized Difference

Senescent Vegetation Index (NDSVI) (Marsett et al., 2006), Normalized Burn Ratio (NBR) (Klemas and Smart, 1983), Modified Normalized Difference Water Index (MNDWI) (Xu, 2006), Normalized Burn Ratio 2 (NBR2) (Miller and Thode, 2007), Normalized Difference Built-up Index (NDBI) (Jin et al., 2015), Shortwave Red Normalized Difference Index (SRNDI) (Zha et al., 2003). Meanwhile, temporal statistics with phenological information, i.e., the standard deviation of NDVI, MNDWI, and NDBI, were used to better depict land covers with temporal fluctuations (e.g., water bodies and vegetation). Additionally, we calculated slope and aspect from GMTD2010 to describe the complex topography.

The RF classifier is widely used for land cover mapping due to its strong anti-noise capability. In particular, RF outperforms other classifiers when dealing with high-dimensional data on a large scale (Gómez et al., 2016). In this study, local adaptive RF classifiers were used where the Arctic was divided into 412 hexagons with side length of 2° . The corresponding local training samples from each region were used to train the RF classifier. Compared with the global model (i.e., mapping the entire Arctic region using all training samples), local RF model can better account for the variety of local landscapes, thus increase mapping accuracy. (Zhang and Roy, 2017). The number of trees for each RF model was set to 200 (Huang et al., 2022b).

3.3. Post-processing

The following post-processing methods were utilized to reduce possible false alarms and improve spatial-temporal consistency. First, we used a potential ISA mask composed of NTL, existing ISA datasets (i.e., WSF2015, GHSL2018, GlobeLand30 2020, and GISA-10m) and OSM to suppress false alarms. Specifically, the Enhanced Vegetation Index

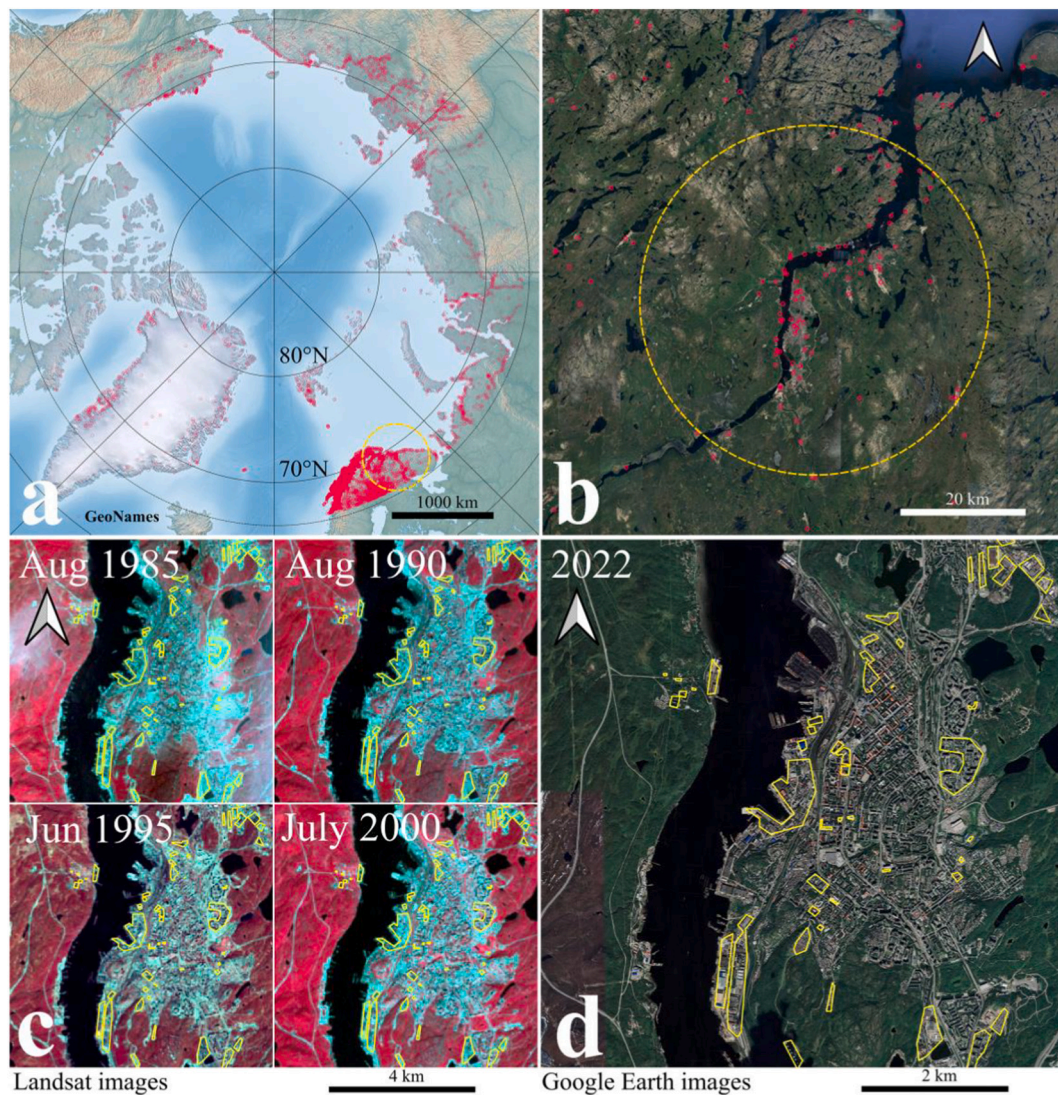


Fig. 2. An example of auxiliary data used for visual interpretation of ISA training samples. (a) distribution of GeoNames in the Arctic Circle, (b) distribution of GeoNames in Murmansk region, (c) drawing of ISA samples based on Landsat, (d) inspection of ISA samples based on Google Earth images.

Table 1
The multi-source features for Arctic annual ISA mapping.

Type	Features	Description	Scale	Dimension	Source
Spectrum	20th,50th,80th: Blue, Green, Red, NIR, SWIR1 and SWIR2	20, 50, 80th percentile value of reflectance from annual Landsat data	30 m	18	Landsat
Spectral indices	20th,50th,80th: NDVI, NDSI, NDSVI, NBR, MNDWI, NBR2, NDBI and SRNDI	NDVI = NI (NIR, Red), NDSI = NI (Green, SWIR1), NDSVI = NI (SWIR1, Red), NBR = NI (NIR, SWIR2), MNDWI = NI (SWIR2, Green), NBR2=NI (SWIR1, SWIR2), NDBI=NI (SWIR1, NIR), SRNDI = NI (SWIR2, Red), where NI represents the function $(b1 - b2) / (b1 + b2)$, b1 and b2 denote two spectral bands	30 m	24	Landsat
Temporal Statistics	NDVI_StdDev, MNDWI_StdDev and NDBI_StdDev	Standard deviation of NDVI, MNDWI and NDBI	30 m	3	Landsat
Terrain	Elevation, slope and aspect	Slope and aspect calculated from the elevation	250 m	3	GMTED

Adjusted Nighttime Light Index (EANTLI) was used to improve the blooming effect phenomenon of NTL (Pok et al., 2017; Zhuo et al., 2018). We investigated the relationship between NTL threshold and

mapping performance to choose the optimal threshold. To this end, we assess the overall accuracy under the different NTL threshold. It is found that the overall accuracy increases as the NTL threshold increases, and

the overall accuracy starts to decrease around the threshold value of 1.6 (Fig. S5). Therefore, we set the NTL threshold as 1.6 in this study. In addition, we made a 500-m buffer for potential ISA mask. Subsequently, we employed a series of post-processing steps, including gap filling, spatial-temporal filtering and sequence temporal reasoning to further improve the spatial-temporal consistency: Gap filling was used to fill in the missing results caused by data availability, cloud cover, and sensor failures. Spatial-temporal filtering was employed to alleviate the “salt and pepper” effect and classification errors. Sequence temporal reasoning was applied to improve pixel labels with temporal logic errors. Overall, these post-processing methods ensure our results become more reasonable and reliable. Readers can refer to (Huang et al., 2021b) for the detailed post-processing strategies.

3.4. Accuracy assessment

The accuracy of GISA_Arctic was evaluated by 37,800 test samples. We employed stratified random sampling to determine the location of ISA and NonISA samples. The distance between each sample was set more than 100 m to ensure their spatial independence. From 1985 to 2021, the test samples were generated by visual interpretation at five-year intervals for a total of eight periods (i.e., 1985, 1990, 1995, 2000, 2005, 2010, 2015 and 2020). To ensure the reliability of samples, the visual interpretation of the test samples was independently carried out by three experts with reference to high-resolution Google Earth and Landsat images. The samples with different labels were removed. The distribution of the test samples is shown in Fig. S1. Finally, the accuracy of GISA_Arctic was reported by overall accuracy (OA), kappa, producer's accuracy (PA), user's accuracy (UA) and F-score. The performance of GISA_Arctic ISA mapping result was further compared with GAIA, GAUD and GISA.

3.5. Land-cover sources for Arctic ISA expansion

Profiting from the long time-series GISA_Arctic, we further explored the sources of the Arctic ISA expansion in the last two decades. Specifically, we overlaid the GlobeLand30 2000 with GISA_Arctic to identify land-cover sources after 2000. These land-cover sources consist of various categories such as cropland, forest, grassland, shrubland, wetlands, water, tundra, bare ground (Chen et al., 2015).

4. Results

4.1. Accuracy assessment

The accuracy of the GISA_Arctic was assessed using 37,800 test samples (Table 2). Overall, GISA_Arctic has the best performance compared with existing products. Specifically, the GISA_Arctic achieved the highest OA of 93.59 %, with an increase of 36.86 %, 39.17 % and 33.99 % with respect to GAIA, GAUD and GISA, respectively. Moreover, the F-score of GISA_Arctic is 0.934, which exceeds GAIA, GAUD and GISA by 0.240, 0.147 and 0.325, respectively. It should be noted that compared with GAIA, GAUD and GISA, the ISA OE of GISA_Arctic is 8.70 %, decreasing by 77.61 %, 83.37 % and 71.83 %, respectively. These findings indicate a notable decrease in omission errors within the Arctic region.

The overall accuracies of GISA_Arctic, GAIA, GAUD and GISA in different periods were calculated. As seen from the Fig. 3, the accuracy of GISA_Arctic produced is significantly higher than other global ISA datasets. This can be attributed to the higher quality, quantity and distribution of the training samples used in GISA_Arctic, compared to the other datasets. These findings highlight the importance and necessity of developing a new Arctic ISA dataset (i.e., GISA_Arctic).

Table 2

Accuracy comparison between GISA_Arctic and other ISA datasets in the Arctic. The OE, CE, and F-score of ISA in each dataset are shown in bold.

GAIA	ISA	NonISA	Precision
ISA	2245	40	98.25 %
NonISA	14,153	16,362	53.62 %
Recall	13.69 %	99.76 %	
OE of ISA	86.31 %	CE of ISA	1.75 %
F-score of ISA	0.240	OA	56.73 %
GAUD	ISA	NonISA	Precision
ISA	1300	28	97.89 %
NonISA	15,098	16,374	52.03 %
Recall	7.93 %	99.83 %	
OE of ISA	92.07 %	CE of ISA	2.11 %
F-score of ISA	0.147	OA	53.88 %
GISA	ISA	NonISA	Precision
ISA	3192	44	98.64 %
NonISA	13,206	16,358	55.33 %
Recall	19.47 %	99.73 %	
OE of ISA	80.53 %	CE of ISA	1.36 %
F-score of ISA	0.325	OA	59.60 %
GISA_Arctic	ISA	NonISA	Precision
ISA	17,253	777	95.69 %
NonISA	1645	18,125	91.68 %
Recall	91.30 %	95.89 %	
OE of ISA	8.70 %	CE of ISA	4.31 %
F-score of ISA	0.934	OA	93.59 %

4.2. Analysis of Arctic ISA

GISA_Arctic has documented the annual ISA dynamics over Arctic regions from 1985 to 2021. During the past 37 years, the Arctic ISA has grown 1.46 times, increasing from 857.83 km² to 2115.49 km². The spatial distribution of ISA in the Arctic in 2021 is shown in Fig. S2 at 0.2° spatial resolution. Northern Europe (Norway, Sweden, Finland) and the western part of Russia are the regions with the highest density of ISA. When examining the density of ISA across the Arctic, it is noteworthy that the northern European countries of Norway, Sweden, Finland, as well as the western part of Russia, exhibit the highest concentration of ISA. Interestingly, despite being the most densely populated region in terms of ISA, Europe has not experienced the most substantial ISA expansion. Instead, the growth has been more rapid in sparsely populated areas characterized by a lower density of ISA. This phenomenon suggests that areas surrounding urban centers and rural regions, which initially have sparser ISA coverage, have witnessed a more pronounced growth of ISA.

The national scale ISA expansion within the Arctic Circle is shown in Fig. S3. The results indicate that over 95 % of the Arctic ISA is occupied by Russia, Norway, Sweden, and Finland. Among them, Russia has the largest ISA, accounting for more than 60 % of the Arctic, while the three Nordic countries (i.e., Norway, Sweden, and Finland) comprise the remaining 35 %. More than 84 % of the Arctic ISA increment is embraced by Russia, Finland, and Norway. The growth rate of ISA in each country has increased significantly over the last decade, with Russia having the highest growth rate of 18.50 km²/year.

Compared to GISA_Arctic, the existing datasets slightly underestimate high-intensity ISA areas (e.g., Murmansk in Fig. 4). However, they exhibit more omissions in low- and medium-intensity ISA areas, such as small and medium-sized cities (e.g., Fig. 5a&b), villages and towns (e.g., Fig. 5c&d). It is also noteworthy that GISA_Arctic extracts more roads, airports, industry and mining areas (e.g., Fig. 5a, b, e&f). Considering the acceleration of Arctic mineral extraction and infrastructure construction in recent years, the GISA_Arctic is more accurate for depicting Arctic ISA dynamics.

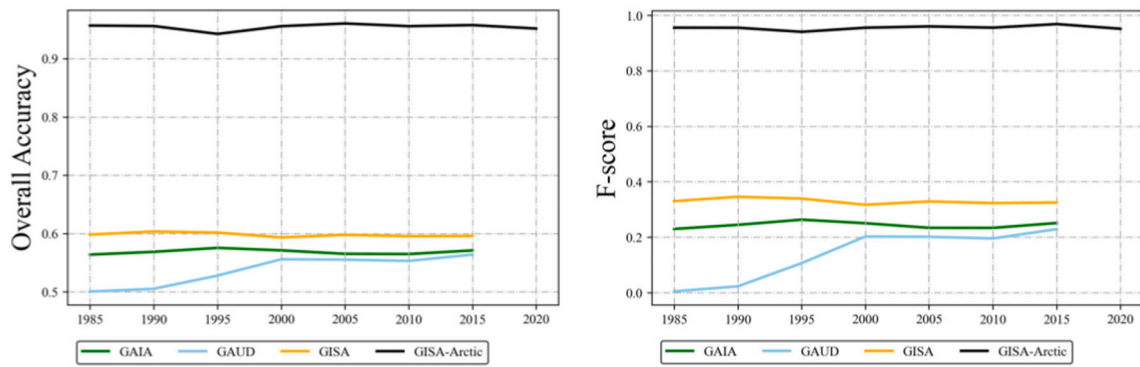


Fig. 3. Overall accuracy and ISA F-score accuracy of GAIA, GAUD, GISA and GISA_Arctic for 1985–2020.

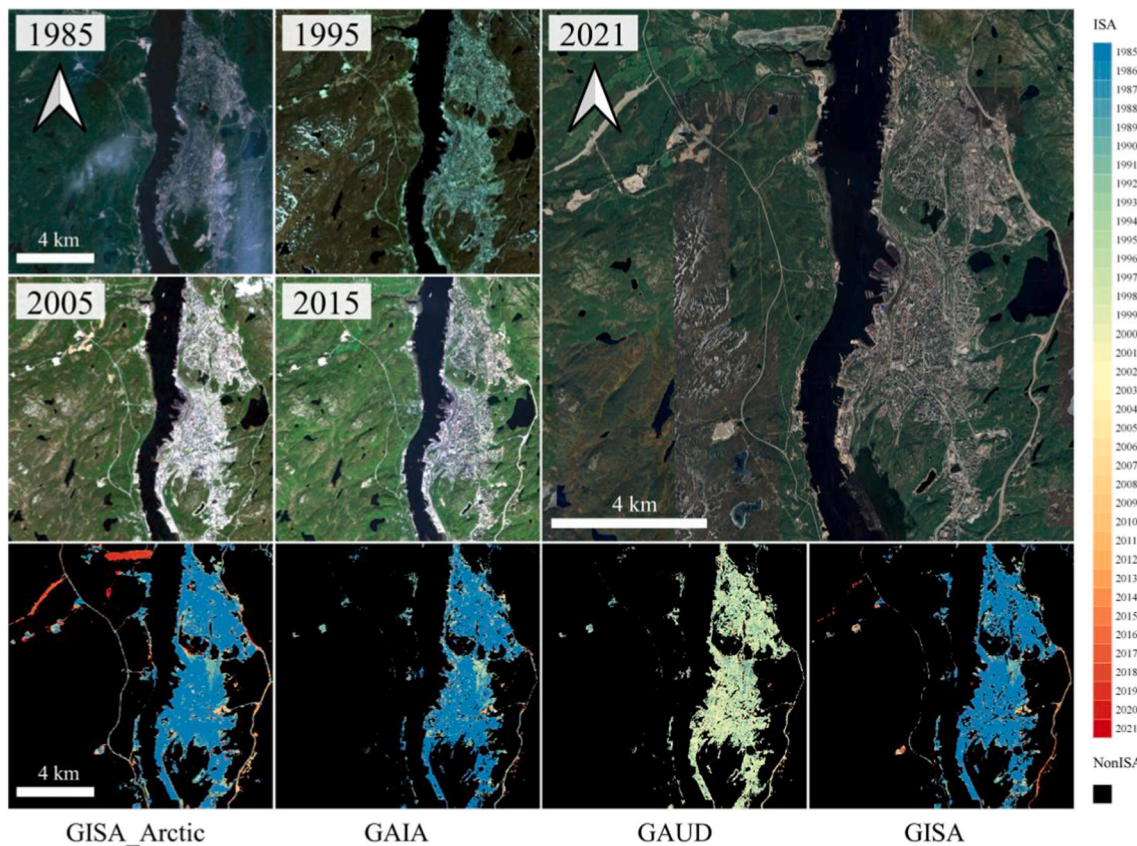


Fig. 4. Comparison of the GISA_Arctic and other time-series ISA datasets in Murmansk.

5. Discussion

5.1. Inter-comparison with existing datasets

In order to better demonstrate the performance of GISA_Arctic, we carried out a comprehensive spatial consistency with established 30-m long time-series global ISA datasets (i.e., GISA, GAIA, GAUD) and the latest 10-m global ISA datasets (i.e., WSF2015, GHSL2018, GISA-10m). To facilitate inter-comparisons across datasets with different resolutions, we calculated the ISA proportion within 0.01° grid (~1 km). Subsequently, the consistency between different datasets was estimated by linear regression of ISA proportion (Fig. S6). Comparatively, scatter plots for GISA, GAIA, and GAUD in relation to GISA_Arctic revealed fitted lines below the 1:1 reference line. This pattern indicates a significant underestimation of ISA extent within the Arctic (Fig. S6). The results also align with the accuracy assessments, wherein ISA omission

rates for GISA, GAIA, and GAUD were higher than that of GISA_Arctic (Table 2). Notably, such underestimation usually occurs in areas characterized by sparse ISA, such as cities, towns, and mining regions (Fig. S7 d-f). In general, the 10-m datasets could capture more ISA benefit from higher spatial resolution. GISA-10m detects more complete roads and mines than GISA_Arctic (Fig. S7 d-f). GHSL2018 and WSF2015, which are more focused on human settlements, detect more accurate buildings than GISA_Arctic (Fig. S7 a, f). Although the existing 10-m datasets outperform GISA_Arctic in terms of depicting fine-scale ISA, such as roads and buildings. GISA_Arctic provides long time-series ISA dynamics that could help understanding the impact of human activities over the Arctic region.

5.2. Arctic ISA mapping

Compared with the other ISA areas (e.g., middle and low latitude

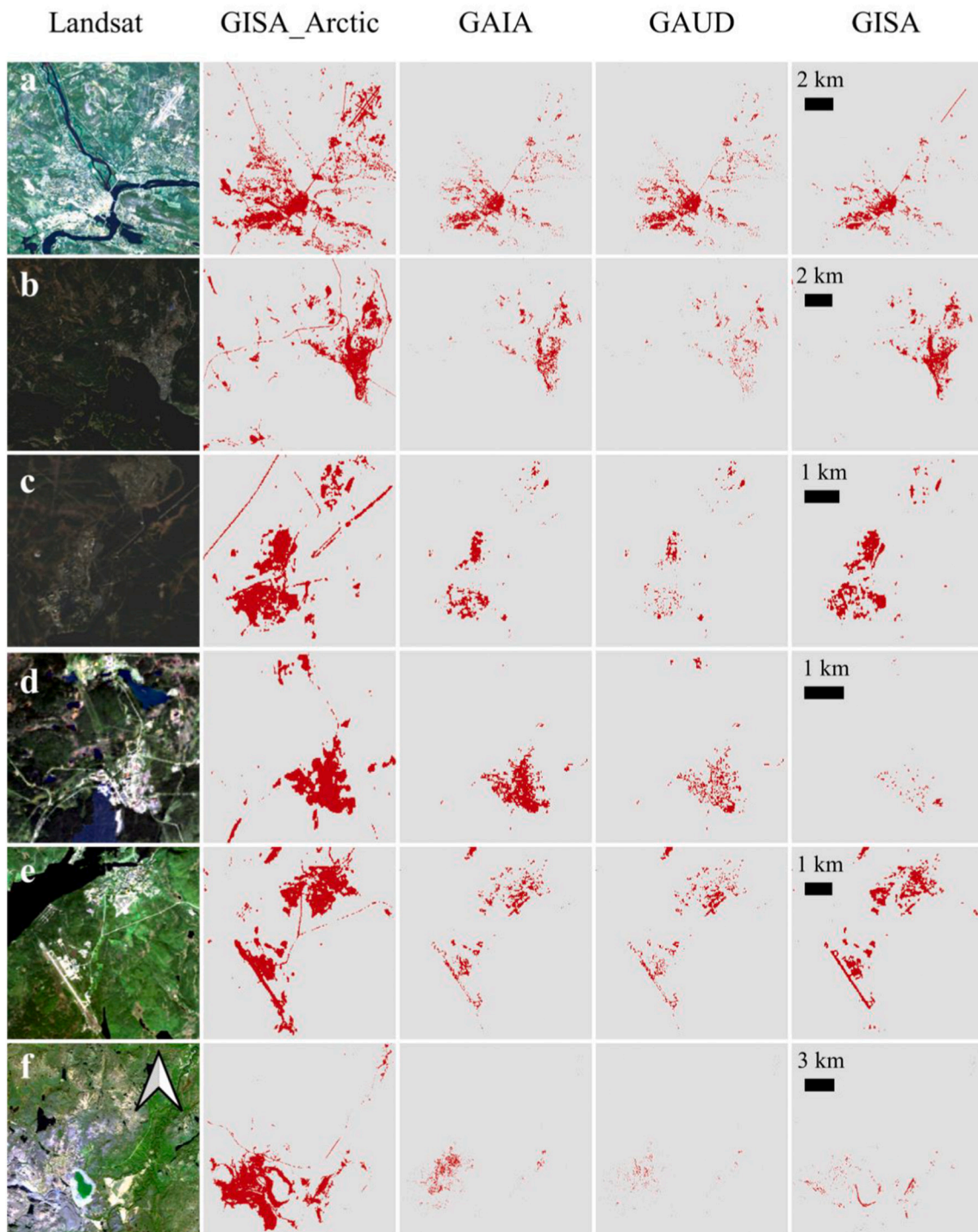


Fig. 5. Comparison of GISA_Arctic with GAIA, GAUD, GISA, GHSL in Rovaniemi (a), Kandalaksha (b), Polyarnye Zori (c), Revada (d), Murmashi (e), Zapolyarny (f).

urban), the Arctic ISA is sparse. While the existing ISA datasets underestimate high-intensity ISA, they exhibit more ISA omissions in the low- and medium-intensity ISA regions (Fig. 4). Conversely, GISA_Arctic extracts more ISA (e.g., roads, mines) than the existing ones (e.g., GISA). Fig. 6 compares the quantity and distribution ISA training sample used in GISA_Arctic and GISA. It was found that GISA_Arctic embraces more and widespread ISA training samples than GISA, which suggests that Arctic ISA mapping could be much improved by combining visually interpreted ISA samples and automatically generated NonISA samples.

In the case of sample acquisition strategy, generating samples from consistent regions of existing datasets has been shown to be efficient and

feasible (e.g., GISA, GAUD)(Huang et al., 2021b; Yang and Huang, 2021). However, the quantity, quality and spatial distribution of the training samples are limited by the datasets used. In general, a combination of automated samples acquired from consistent areas and visually-interpreted samples from inconsistent areas can effectively improve mapping performance (Huang et al., 2022a). In the Arctic region, ISA mapping remains challenging due to issues such as the short summer sunlight duration and the limited viewing zenith angle. Furthermore, existing datasets exhibit significant underestimation. These issues constrain the reliability and feasibility of automatic sample acquisition in the Arctic. Therefore, we employed visually interpreted

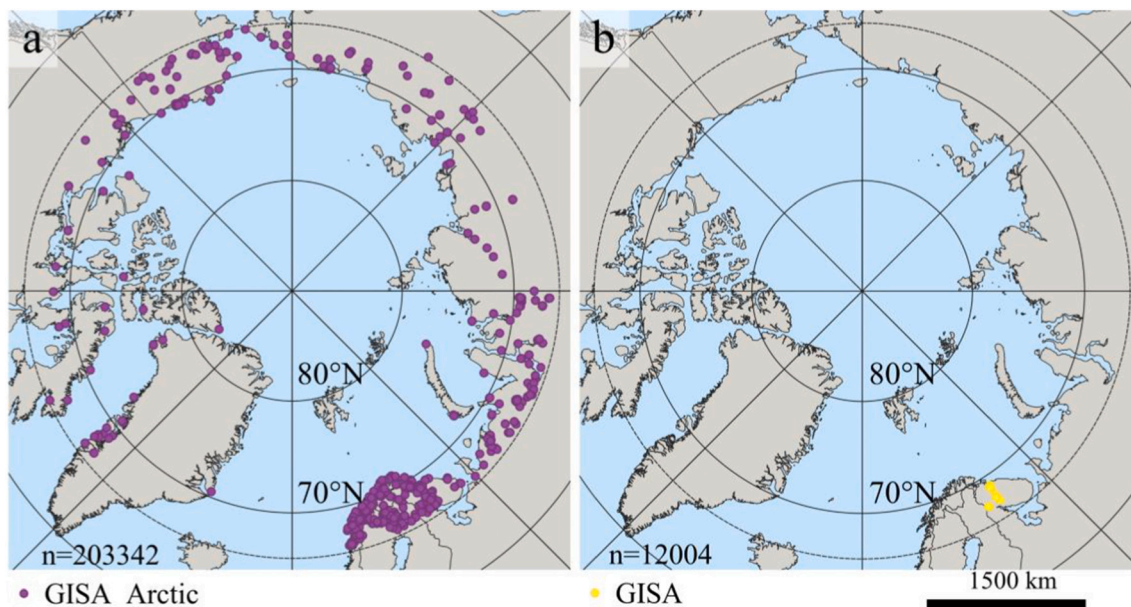


Fig. 6. ISA training samples of GISA_Arctic and GISA in the Arctic for 2015. (a) ISA training sample distribution of GISA_Arctic, (b) ISA training sample distribution of GISA, n represents the number of ISA samples.

ISA samples and automatically generated NonISA samples for GISA_Arctic. In addition, we used GeoNames and OSM to locate potential ISA, which significantly reduced the time required for interpreting ISA samples.

5.3. Land-use sources of Arctic ISA

We further analyzed the sources of ISA expansion in the Arctic from 2001 to 2021 (Fig. 7). Considering that bare land and glacier accounts for less than 1 % of ISA expansion, they were excluded in the analysis. Tundra, woodland, and grassland, were found to be the primary sources of ISA expansion, accounting for more than 80 % of the total. Contrarily, the cultivated land, wetland, and water together account for less than 10 %. Notably, our analysis highlights that Russia significantly contributes the largest annual growth of ISA in the Arctic. This contribution

is accompanied by a further increase in the proportion of tundra, forest, and grassland, while the relative share of cultivated land, wetland, and water decreases (Fig. S4).

It can be seen that ISA expansion usually occurs in urban fringe (Fig. 8a-c), port and infrastructure construction sites (Fig. 8d), industrial development areas (Fig. 8e&f) and mining areas (Fig. 8g&h). Among the Arctic countries, the most significant ISA expansion has occurred in Russia and the Nordic region. The main drivers of continued ISA expansion are mineral exploitation, energy development, settlement expansion and infrastructure construction (Melia et al., 2016). The extent of Arctic sea ice has decreased since 1980 due to the global warming, making natural resources such as oil and gas more accessible at higher latitudes, contributing to increased Arctic shipping volumes (Mudryk et al., 2021). The development of Arctic shipping routes, such as the Northwest Passage, the Northern Sea Route, and the Trans-Polar

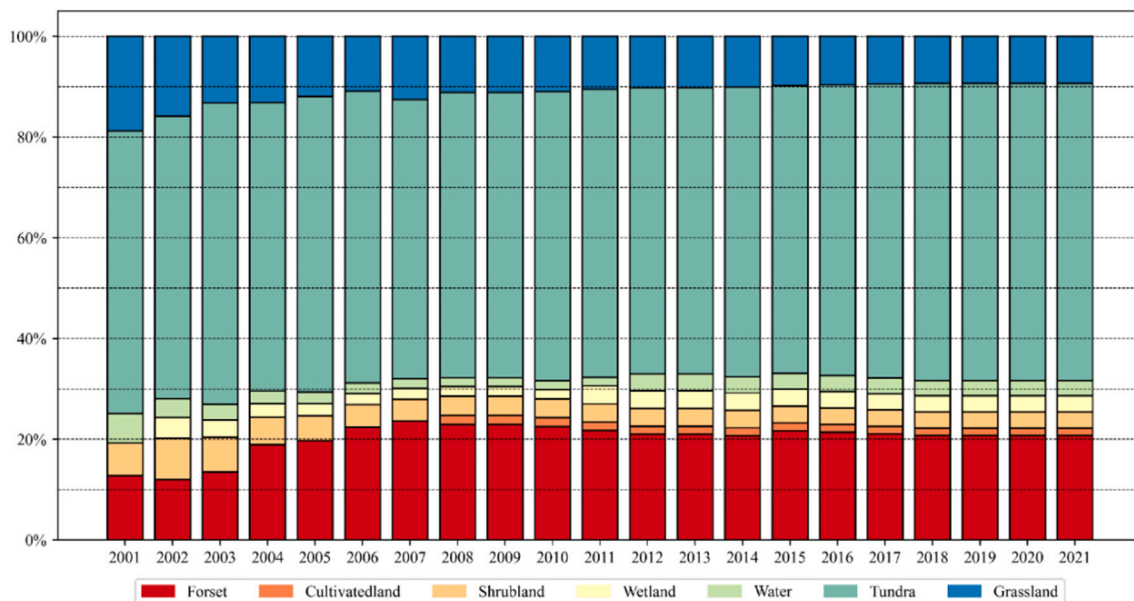


Fig. 7. Land-use sources for ISA in the Arctic for 2001–2021.



Fig. 8. Examples of land-cover sources of ISA expansion in 2001–2021. (a) Belokamenka, (b) Rovaniemi, (c) near North Murmansk, (d) Sabelta, (e) near Hammerfest, (f) near Nosovaya, (g) near Kaunisvaara, (h) near Petkura.

Sea Route, has led to more petroleum exploitation and ship transportation, resulting in ISA growth in mines and ports (Stephenson et al., 2011) (Melia et al., 2016). In general, various industrial developments focus on energy sources (e.g., power stations, steel mills) and transportation continue to accelerate the ISA expansion over the Arctic region.

6. Conclusions

This study developed the first Arctic ISA dataset (GISA_Arctic) for the Arctic Circle (i.e., regions with latitudes greater than $66^{\circ}34'N$) from 1985 to 2021. For this purpose, toponymic data such as GeoNames are used to collect high-quality and widely distributed training samples. This provides a reference for quickly collecting high reliability samples in areas with sparse and uneven distribution of ISA. Based on the 337,799 Landsat images on the GEE platform, multi-source features, such as spectrum, spectral indices, phenology and topographic features

were fed to local adaptive RF classifiers. Based on 37,800 test samples, the OE, CE and F-score of GISA_Arctic are 8.70 %, 4.31 % and 0.934, respectively, which outperforms existing ISA datasets. GISA_Arctic significantly reduces ISA omission compared to existing datasets, enabling better monitoring of Arctic ISA dynamics.

Courtesy of GISA_Arctic, we analyzed the ISA dynamics in the Arctic from 1985 to 2021. The Arctic ISA expanded from 857.83 km² to 2115.49 km² during this period, with over 84 % of Arctic ISA increment is embraced by Russia, Finland, and Norway. The analysis on land covers transformed to ISA is also presented in this research. It was found that more than 80 % of the ISA gain stems from forest, tundra and grassland after 2000, which may be contributed to the development of transportation, industrial construction, expansion of residential areas, and mining of mineral resources. Given the intensive ecological changes associated with global warming, the long time-series ISA dynamics provided by GISA_Arctic will enhance our understanding of human in north polar.

Declaration of competing interest

The authors declare that they have no known competing financial interests or personal relationships that could have appeared to influence the work reported in this paper.

Data availability

Data will be made available on request.

Acknowledgement

The research was supported by the National Natural Science Foundation of China (under Grants 41971295 and 42271328).

CRedit authorship contribution statement

Jie Yang: Conceptualization, Methodology, Writing-Reviewing and Editing. Zhengrong Liu: Software, Validation, Writing- Original draft preparation. Xin Huang: Conceptualization, Supervision, Writing-Reviewing and Editing.

Appendix A. Supplementary data

Supplementary data to this article can be found online at <https://doi.org/10.1016/j.scitotenv.2023.166966>.

References

- Assessment, A.C.I., 2005. *Arctic Climate Impact Assessment*. Cambridge University Press Cambridge.
- Beamish, A., Reynolds, M.K., Epstein, H., Frost, G.V., Macander, M.J., Bergstedt, H., Bartsch, A., Kruse, S., Miles, V., Tanis, C.M., Heim, B., Fuchs, M., Chabrilat, S., Shevtsova, I., Verdonen, M., Wagner, J., 2020. Recent trends and remaining challenges for optical remote sensing of Arctic tundra vegetation: a review and outlook. *Remote Sens. Environ.* 246, 111872. <https://doi.org/10.1016/j.rse.2020.111872>.
- Chen, Jun, Chen, Jin, Liao, A., Cao, X., Chen, L., Chen, X., He, C., Han, G., Peng, S., Lu, M., Zhang, W., Tong, X., Mills, J., 2015. Global land cover mapping at 30m resolution: a POK-based operational approach. *ISPRS J. Photogramm. Remote Sens. Glob. Land Cover Map. Monit.* 103, 7–27. <https://doi.org/10.1016/j.isprsjprs.2014.09.002>.
- Chen, X., Jeong, S., Park, C.-E., Park, H., Joo, J., Chang, D., Yun, J., 2022. Different responses of surface freeze and thaw phenology changes to warming among Arctic permafrost types. *Remote Sens. Environ.* 272, 112956. <https://doi.org/10.1016/j.rse.2022.112956>.
- Clinton, N., Gong, P., 2013. MODIS detected surface urban heat islands and sinks: global locations and controls. *Remote Sens. Environ.* 134, 294–304 ([doi:10.1016/j.rse.2012.11.016](https://doi.org/10.1016/j.rse.2012.11.016)).
- Corbane, C., Syrris, V., Sabo, F., Politis, P., Melchiorri, M., Pesaresi, M., Soille, P., Kemper, T., 2021. Convolutional neural networks for global human settlements mapping from Sentinel-2 satellite imagery. *Neural Comput. & Applic.* 33, 6697–6720. <https://doi.org/10.1007/s00521-020-05449-7>.
- Elvidge, C.D., Baugh, K., Zhizhin, M., Hsu, F.C., Ghosh, T., 2017. VIIRS night-time lights. *Int. J. Remote Sens.* 38, 5860–5879. <https://doi.org/10.1080/01431161.2017.1342050>.
- Fonte, C.C., Patriarca, J., Jesus, I., Duarte, D., 2020. Automatic extraction and filtering of OpenStreetMap data to generate training datasets for land use land cover classification. *Remote Sens.* <https://doi.org/10.3390/rs12203428>.
- Goetz, M., 2013. Towards generating highly detailed 3D CityGML models from OpenStreetMap. *Int. J. Geogr. Inf. Sci.* 27, 845–865. <https://doi.org/10.1080/13658816.2012.721552>.
- Gómez, C., White, J.C., Wulder, M.A., 2016. Optical remotely sensed time series data for land cover classification: a review. *ISPRS J. Photogramm. Remote Sens.* 116, 55–72. <https://doi.org/10.1016/j.isprsjprs.2016.03.008>.
- Gong, P., Li, X., Wang, J., Bai, Y., Chen, B., Hu, T., Liu, X., Xu, B., Yang, J., Zhang, W., Zhou, Y., 2020. Annual maps of global artificial impervious area (GAIA) between 1985 and 2018. *Remote Sens. Environ.* 236, 111510. <https://doi.org/10.1016/j.rse.2019.111510>.
- Gorelick, N., Hancher, M., Dixon, M., Ilyushchenko, S., Thau, D., Moore, R., 2017. Google Earth Engine: planetary-scale geospatial analysis for everyone. In: *Remote Sensing of Environment, Big Remotely Sensed Data: Tools, Applications and Experiences*, 202, pp. 18–27. <https://doi.org/10.1016/j.rse.2017.06.031>.
- Guo, W., Liu, H., Anenkhonov, O.A., Shangguan, H., Sandanov, D.V., Korolyuk, A.Yu., Hu, G., Wu, X., 2018. Vegetation can strongly regulate permafrost degradation at its southern edge through changing surface freeze-thaw processes. *Agric. For. Meteorol.* 252, 10–17. <https://doi.org/10.1016/j.agrformet.2018.01.010>.
- Haklay, M., Weber, P., 2008. OpenStreetMap: user-generated street maps. *IEEE Pervasive Comput.* 7, 12–18. <https://doi.org/10.1109/MPRV.2008.80>.
- Hall, D.K., Riggs, G.A., Salomonson, V.V., 1995. Development of methods for mapping global snow cover using moderate resolution imaging spectroradiometer data. *Remote Sens. Environ.* 54, 127–140. [https://doi.org/10.1016/0034-4257\(95\)00137-P](https://doi.org/10.1016/0034-4257(95)00137-P).
- Hermosilla, T., Wulder, M.A., White, J.C., Coops, N.C., 2019. Prevalence of multiple forest disturbances and impact on vegetation regrowth from interannual Landsat time series (1985–2015). *Remote Sens. Environ.* 233, 111403. <https://doi.org/10.1016/j.rse.2019.111403>.
- Huang, X., Huang, J., Wen, D., Li, J., 2021a. An updated MODIS global urban extent product (MGUP) from 2001 to 2018 based on an automated mapping approach. *Int. J. Appl. Earth Obs. Geoinf.* 95, 102255. <https://doi.org/10.1016/j.jag.2020.102255>.
- Huang, X., Li, J., Yang, J., Zhang, Z., Li, D., Liu, X., 2021b. 30 m global impervious surface area dynamics and urban expansion pattern observed by Landsat satellites: from 1972 to 2019. *Sci. China Earth Sci.* 64, 1922–1933 ([doi:10.1016/j.sces.2021.05.001](https://doi.org/10.1016/j.sces.2021.05.001)).
- Huang, X., Song, Y., Yang, J., Wang, W., Ren, H., Dong, M., Feng, Y., Yin, H., Li, J., 2022a. Toward accurate mapping of 30-m time-series global impervious surface area (GISA). *Int. J. Appl. Earth Obs. Geoinf.* 109, 102787. <https://doi.org/10.1016/j.jag.2022.102787>.
- Huang, X., Yang, J., Wang, W., Liu, Z., 2022b. Mapping 10-m global impervious surface area (GISA-10m) using multi-source geospatial data. *Earth Syst. Sci. Data Discuss.* 1–39. <https://doi.org/10.5194/essd-2021-458>.
- Jin, X., Ma, J., Wen, Z., Song, K., 2015. Estimation of maize residue cover using Landsat-8 OLI image spectral information and textural features. *Remote Sens.* 7, 14559–14575. <https://doi.org/10.3390/rs71114559>.
- Klemes, V., Smart, R., 1983. The influence of soil salinity, growth form, and leaf moisture on the spectral radiance of Photogramm. *Eng. Remote Sens. (Basel)* 49, 77–83.
- Li, X., Gong, P., 2016. An “exclusion-inclusion” framework for extracting human settlements in rapidly developing regions of China from Landsat images. *Remote Sens. Environ.* 186, 286–296. <https://doi.org/10.1016/j.rse.2016.08.029>.
- Lifshits, S., Glyaznetsova, Y., Erofeevskaya, L., Chalaya, O., Zueva, I., 2021. Effect of oil pollution on the ecological condition of soils and bottom sediments of the arctic region (Yakutia). *Environ. Pollut.* 288, 117680. <https://doi.org/10.1016/j.envpol.2021.117680>.
- Lin, Y., Zhang, H., Lin, H., Gamba, P.E., Liu, X., 2020. Incorporating synthetic aperture radar and optical images to investigate the annual dynamics of anthropogenic impervious surface at large scale. *Remote Sens. Environ.* 242, 111757. <https://doi.org/10.1016/j.rse.2020.111757>.
- Liu, Z., He, C., Zhang, Q., Huang, Q., Yang, Y., 2012. Extracting the dynamics of urban expansion in China using DMSP-OLS nighttime light data from 1992 to 2008. *Landsc. Urban Plan.* 106, 62–72. <https://doi.org/10.1016/j.landurbplan.2012.02.013>.
- Liu, X., Huang, Y., Xu, X., Li, Xuecao, Li, Xia, Ciais, P., Lin, P., Gong, K., Ziegler, A.D., Chen, A., Gong, P., Chen, J., Hu, G., Chen, Y., Wang, S., Wu, Q., Huang, K., Estes, L., Zeng, Z., 2020. High-spatiotemporal-resolution mapping of global urban change from 1985 to 2015. *Nat. Sustain.* 3, 564–570 ([doi:10.1038/s41597-020-0107-6](https://doi.org/10.1038/s41597-020-0107-6)).
- Marconcini, M., Metz-Marconcini, A., Üreyen, S., Palacios-Lopez, D., Hanke, W., Baçofer, F., Zeidler, J., Esch, T., Gorelick, N., Kakarla, A., Paganini, M., Strano, E., 2020. Outlining where humans live, the world settlement footprint 2015. *Sci. Data* 7, 242. <https://doi.org/10.1038/s41597-020-00580-5>.
- Marsett, R.C., Qi, J., Heilman, P., Biedenbender, S.H., Carolyn Watson, M., Amer, S., Weltz, M., Goodrich, D., Marsett, R., 2006. Remote sensing for grassland management in the arid Southwest. *Rangel. Ecol. Manag.* 59, 530–540. <https://doi.org/10.2111/05-201R.1>.
- McGuire, A.D., Anderson, L.G., Christensen, T.R., Dallimore, S., Guo, L., Hayes, D.J., Heimann, M., Lorenson, T.D., Macdonald, R.W., Roulet, N., 2009. Sensitivity of the carbon cycle in the Arctic to climate change. *Ecol. Monogr.* 79, 523–555. <https://doi.org/10.1890/08-2025.1>.
- Melia, N., Haines, K., Hawkins, E., 2016. Sea ice decline and 21st century trans-Arctic shipping routes. *Geophys. Res. Lett.* 43, 9720–9728. <https://doi.org/10.1002/2016GL069315>.
- Miller, J.D., Thode, A.E., 2007. Quantifying burn severity in a heterogeneous landscape with a relative version of the delta Normalized Burn Ratio (dNBR). *Remote Sens. Environ.* 109, 66–80. <https://doi.org/10.1016/j.rse.2006.12.006>.
- Mills, S., Weiss, S., Liang, C., 2013. VIIRS day/night band (DNB) stray light characterization and correction. In: *Earth Observing Systems XVIII*. Presented at the Earth Observing Systems XVIII, SPIE, pp. 549–566. <https://doi.org/10.1117/12.2023107>.
- Mudryk, L.R., Dawson, J., Howell, S.E.L., Derksen, C., Zagon, T.A., Brady, M., 2021. Impact of 1, 2 and 4 °C of global warming on ship navigation in the Canadian Arctic. *Nat. Clim. Chang.* 11, 673–679. <https://doi.org/10.1038/s41558-021-01087-6>.
- Nguyen, T.L.H., Park, S.-H., Yeo, G.-T., 2021. Keyword network analysis: uncovering research trends on the Northern Sea Route. *Asian J. Ship. Logist.* 37, 231–238. <https://doi.org/10.1016/j.ajsl.2021.06.001>.
- Overland, J.E., Wang, M., Walsh, J.E., Stroeve, J.C., 2014. Future Arctic climate changes: adaptation and mitigation time scales. *Earth's Future* 2, 68–74. <https://doi.org/10.1002/2013EF000162>.
- Pok, S., Matsushita, B., Fukushima, T., 2017. An easily implemented method to estimate impervious surface area on a large scale from MODIS time-series and improved DMSP-OLS nighttime light data. *ISPRS J. Photogramm. Remote Sens.* 133, 104–115. <https://doi.org/10.1016/j.isprsjprs.2017.10.005>.
- Rouse Jr., J.W., Haas, R.H., Schell, J., Deering, D., 1973. *Monitoring the Vernal Advancement and Retrogradation (Green Wave Effect) of Natural Vegetation*.
- Schmidt, G.L., Jenkerson, C., Masek, J.G., Vermote, E., Gao, F., 2013. Landsat Ecosystem Disturbance Adaptive Processing System (LEDAPS) Algorithm Description. <https://doi.org/10.3133/ofr20131057>.

- Schneider, A., Friedl, M.A., Potere, D., 2010. Mapping global urban areas using MODIS 500-m data: New methods and datasets based on 'urban ecoregions'. *Remote Sens. Environ.* 114, 1733–1746 (doi:10/dd4zzg).
- Schuur, E.A., McGuire, A.D., Schädel, C., Grosse, G., Harden, J.W., Hayes, D.J., Hugelius, G., Koven, C.D., Kuhry, P., Lawrence, D.M., 2015. Climate change and the permafrost carbon feedback. *Nature* 520, 171–179. <https://doi.org/10.1038/nature14338>.
- Seto, K.C., Güneralp, B., Hutyra, L.R., 2012. Global forecasts of urban expansion to 2030 and direct impacts on biodiversity and carbon pools. *Proc. Natl. Acad. Sci.* 109, 16083–16088. <https://doi.org/10.1073/pnas.1211658109>.
- Sexton, J.O., Song, X.-P., Huang, C., Channan, S., Baker, M.E., Townshend, J.R., 2013. Urban growth of the Washington, D.C.–Baltimore, MD metropolitan region from 1984 to 2010 by annual, Landsat-based estimates of impervious cover. *Remote Sens. Environ.* 129, 42–53. <https://doi.org/10.1016/j.rse.2012.10.025>.
- Stephenson, S.R., Smith, L.C., Agnew, J.A., 2011. Divergent long-term trajectories of human access to the Arctic. *Nat. Clim. Chang.* 1, 156–160. <https://doi.org/10.1038/nclimate1120>.
- Tian, Y., Zhou, Q., Fu, X., 2019. An analysis of the evolution, completeness and spatial patterns of OpenStreetMap building data in China. *ISPRS Int. J. Geo Inf.* <https://doi.org/10.3390/ijgi8010035>.
- Usman, M., Jahanger, A., Makhdom, M.S.A., Balsalobre-Lorente, D., Bashir, A., 2022. How do financial development, energy consumption, natural resources, and globalization affect Arctic countries' economic growth and environmental quality? An advanced panel data simulation. *Energy* 241, 122515. <https://doi.org/10.1016/j.energy.2021.122515>.
- Vermote, E., Justice, C., Claverie, M., Franch, B., 2016. Preliminary analysis of the performance of the Landsat 8/OLI land surface reflectance product. In: *Remote Sensing of Environment, Landsat 8 Science Results*, 185, pp. 46–56. <https://doi.org/10.1016/j.rse.2016.04.008>.
- Weng, Q., 2012. Remote sensing of impervious surfaces in the urban areas: requirements, methods, and trends. In: *Remote Sensing of Environment, Remote Sensing of Urban Environments*, 117, pp. 34–49 (doi:10/csfws9).
- Xu, H., 2006. Modification of normalised difference water index (NDWI) to enhance open water features in remotely sensed imagery. *Int. J. Remote Sens.* 27, 3025–3033. <https://doi.org/10.1080/01431160600589179>.
- Yang, J., Huang, X., 2021. The 30m annual land cover dataset and its dynamics in China from 1990 to 2019. *Earth Syst. Sci. Data* 13, 3907–3925. <https://doi.org/10.5194/essd-13-3907-2021>.
- Zha, Y., Gao, J., Ni, S., 2003. Use of normalized difference built-up index in automatically mapping urban areas from TM imagery. *Int. J. Remote Sens.* 24, 583–594. <https://doi.org/10.1080/01431160304987>.
- Zhang, H.K., Roy, D.P., 2017. Using the 500m MODIS land cover product to derive a consistent continental scale 30m Landsat land cover classification. *Remote Sens. Environ.* 197, 15–34. <https://doi.org/10.1016/j.rse.2017.05.024>.
- Zhang, L., Weng, Q., Shao, Z., 2017. An evaluation of monthly impervious surface dynamics by fusing Landsat and MODIS time series in the Pearl River Delta, China, from 2000 to 2015. *Remote Sens. Environ.* 201, 99–114. <https://doi.org/10.1016/j.rse.2017.08.036>.
- Zhou, Y., Li, X., Asrar, G.R., Smith, S.J., Imhoff, M., 2018. A global record of annual urban dynamics (1992–2013) from nighttime lights. *Remote Sens. Environ.* 219, 206–220 (doi:10/gfp5m8).
- Zhu, Z., Wang, S., Woodcock, C.E., 2015. Improvement and expansion of the Fmask algorithm: cloud, cloud shadow, and snow detection for Landsats 4–7, 8, and Sentinel 2 images. *Remote Sens. Environ.* 159, 269–277. <https://doi.org/10.1016/j.rse.2014.12.014>.
- Zhuo, L., Shi, Q., Tao, H., Zheng, J., Li, Q., 2018. An improved temporal mixture analysis unmixing method for estimating impervious surface area based on MODIS and DMSP-OLS data. *ISPRS J. Photogramm. Remote Sens.* 142, 64–77. <https://doi.org/10.1016/j.isprsjprs.2018.05.016>.